




Radiation effects in ultra-thin GaAs solar cells

Cite as: J. Appl. Phys. **132**, 184501 (2022); doi: [10.1063/5.0103381](https://doi.org/10.1063/5.0103381)

Submitted: 15 June 2022 · Accepted: 4 October 2022 ·

Published Online: 8 November 2022



A. Barthel,^{1,a)}  L. Sayre,¹  G. Kusch,¹  R. A. Oliver,¹  and L. C. Hirst^{1,2} 

AFFILIATIONS

¹Department of Materials Science and Metallurgy, University of Cambridge, Cambridge CB3 0FS, United Kingdom

²Department of Physics, University of Cambridge, Cambridge CB3 0HE, United Kingdom

Note: This paper is part of the Special Topic on Radiation Effects in Materials.

a) Author to whom correspondence should be addressed: ab2301@cam.ac.uk

ABSTRACT

Ultra-thin solar cells are of significant interest for use in space due to their intrinsic radiation tolerance, which may allow them to be used in particularly harsh radiation environments, where thicker cells would degrade rapidly and enable reduction in cover glass thickness to reduce launch mass. In this study, devices with an 80 nm GaAs absorber layer were irradiated with 3 MeV protons. It is shown that integrated light management in these ultra-thin devices offers enhanced efficiency, in addition to extended lifetime through radiation resilience. Time-resolved cathodoluminescence is employed to map the introduction of radiation-induced defects with increasing proton fluence and characterize a decrease in carrier lifetime from 198 ± 5 ps pre-radiation to 6.2 ± 0.6 ps, after irradiation to 2×10^{14} cm⁻² fluence. Despite the substantial reduction in carrier lifetime, short-circuit current does not degrade up to a proton fluence of 1×10^{15} cm⁻², beyond which a collapse in short-circuit current is observed. This exposure correlates with the point at which the carrier lifetime, extrapolated from cathodoluminescence, becomes comparable to the transit time for carriers to cross the ultra-thin device. Variation in current-voltage behavior with carrier lifetime and fluence shows that the recombination statistics are similar to those of a Shockley-Read-Hall single deep-level trap model, but that bimolecular recombination does not fully describe the observed behavior. An implication of these highly radiation tolerant cells for space power systems is shown to offer significant savings in cover glass mass, compared with a thicker cell.

© 2022 Author(s). All article content, except where otherwise noted, is licensed under a Creative Commons Attribution (CC BY) license (<http://creativecommons.org/licenses/by/4.0/>). <https://doi.org/10.1063/5.0103381>

I. INTRODUCTION

The majority of space satellites rely on photovoltaic cells for power. Space is a harsh environment and satellites encounter a variety of hazards on orbit.^{1–3} One of the most problematic for solar cells is corpuscular radiation, particularly energetic protons and electrons. Radiation exposure gradually damages solar cells, causing their performance to degrade, which, depending on the orbit, may limit a satellite's lifetime.^{4–8}

Irradiation causes damage by displacing atoms. In the crystalline semiconductors that are predominantly used for space photovoltaics, a large fraction of the displaced atoms become defects.^{4,9} These defects often introduce states within the bandgap of the semiconductor and act as recombination centres, reducing the minority carrier lifetime of the material.^{4,10,11} A reduction in minority carrier lifetime translates into reduction in minority carrier diffusion length, which, respectively, corresponds to reduction in photovoltage and photocurrent and, therefore, the power output of the solar cell.^{4–6}

The rate and severity of the damage induced are dependent on a large number of factors including particle flux, species, and kinetic energy. These factors can vary greatly for different space environments, as shown in Fig. 1, which compares differential proton flux as a function of energy for a number of Earth orbits and the orbit of Jupiter's moon Europa. These data were acquired by simulating the radiation environments of the respective orbits using SPENVIS¹². The proton flux encountered on the highly eccentric Molniya orbit^{13,14} is significantly greater than for the other Earth orbits depicted, because the Molniya orbit passes through the center of the Earth's proton radiation belt, while the others are at its outskirts. This is one reason that middle Earth orbits (MEO), including highly eccentric orbits, like Molniya, are not commonly used. The high radiation flux results in high degradation rates of the satellite's photovoltaic power supply, cutting down on the mission lifetime and driving up costs.^{5,15} However, MEO have a lot of potential,^{13,16,17} and will become more lucrative as low Earth orbit becomes cluttered.^{18–20} It is, therefore, necessary

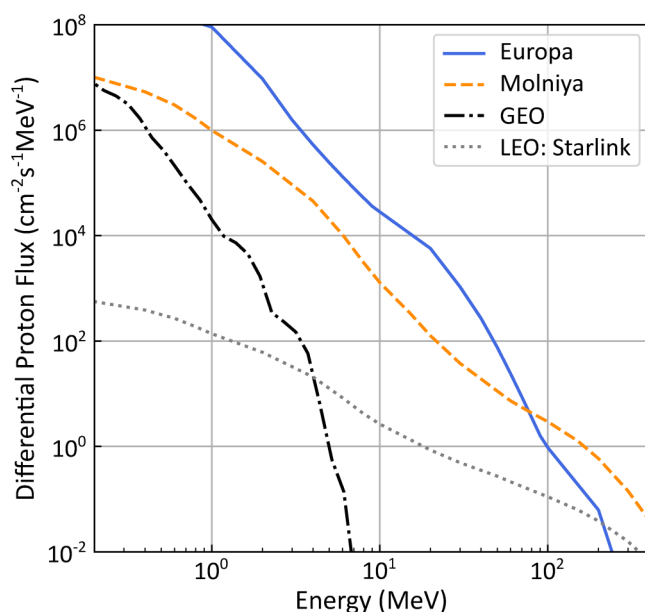


FIG. 1. Variation of differential proton flux with proton energy for four different Earth orbits and the orbit of Jupiter's moon Europa. The Earth orbits include the Molniya orbit, which is an example of a highly eccentric middle Earth orbit and examples of the most commonly used orbits, namely, low Earth orbits (LEO) and geostationary orbit (GEO).

to develop space photovoltaics with greater radiation tolerance that can extend mission lifetimes in MEO. Another area of interest for highly radiation tolerant photovoltaics is exploration of other planets and their moons. Europa, in particular, has garnered significant scientific interest.^{21,22} However, it orbits in one of the most severe planetary radiation environments in the solar system and has no atmosphere.²³ As such, a solar powered lander²² would benefit greatly from high radiation tolerance.

Several possibilities exist for improving the radiation tolerance of solar cells. This study focuses on an intrinsically radiation tolerant cell design using an ultra-thin absorber layer. This builds on an existing approach for improving radiation tolerance, which has been to reduce the thickness of the device.^{11,24–27} In doing so, the distance photo-excited carriers need to travel to reach the bounding carrier selective layers is reduced, such that the onset of short-circuit current degradation due to radiation-induced minority carrier diffusion length degradation is delayed. While the diffusion length remains greater than the layer thickness, the short-circuit current will not be affected by changes in diffusion length. The ultra-thin solar cell (UTSC) design fully capitalizes on this form of radiation tolerance²⁶ using absorber layer thicknesses that are orders of magnitude below the initial diffusion length. If the absorber layer is made sufficiently thin, it may even become fully depleted under short-circuit conditions, in which case all photo-generated carriers will be swept to the contacts by the electric field and the short-circuit current will be unaffected by changes in the carrier recombination rate. As a result, these cells may be subjected

to high doses of radiation and the absorber material may become highly damaged before a degradation in short-circuit current is expected. Under open-circuit conditions, the defects introduced will still act to suppress the induced voltage, as with a conventional, thicker cell.⁴

While the enhanced radiation tolerance of ultra-thin cells has been demonstrated,²⁶ this needs to be coupled with an improvement in beginning-of-life performance. Inherent drawbacks of the ultra-thin design are high transmission losses and a greater impact from surface recombination compared to thicker cells. These can be mitigated by the integration of light management structures^{28,29} and optimized passivation layers.^{28,30}

Furthermore, improved understanding of the physical behavior of these cells, including the correlation of material properties with device performance as a function of radiation damage, is sought.

In this study, ultra-thin GaAs solar cells, both with and without integrated light management, were irradiated with 3 MeV protons to a range of fluences and the variation of material and device parameters with fluence was measured. Device parameters were obtained by measuring the current–voltage characteristics of the cells in the dark (DIV) and under 1-sun AM0 illumination (LIV). An enhanced performance over previously reported devices, while maintaining no degradation in short-circuit current up to high fluences, was observed. The effect of radiation on the absorber material was investigated using cathodoluminescence (CL) imaging. By collecting time-resolved CL (TRCL) intensity, the minority carrier lifetime of the material could be extracted. The measured lifetime was compared with the calculated transit time of carriers moving across the junction, yielding an explanation for the collapse in short-circuit current observed at very high fluence. The analysis of the current–voltage behavior of the cells and its variation with fluence and measured carrier lifetime was carried out, and the applicability of conventional recombination statistics to this ultra-thin geometry is discussed. Finally, the implications of these ultra-thin cells for space power systems are considered.

II. EXPERIMENTAL METHODS

A. Sample fabrication

Ultra-thin GaAs solar cells with an 80 nm absorber were fabricated. The length scale was selected to allow for direct comparison with the previous work, where intrinsic radiation tolerance has been demonstrated.²⁶ The device layer structure was grown on a p-type GaAs substrate using molecular beam epitaxy (Table I). This layer structure was processed to yield both on-wafer and off-wafer devices, with the latter inverting the layer structure and incorporating a planar silver back mirror to enhance light absorption. In this ultra-thin regime, surface effects could lead to undesirable depletion region recombination and a reduction in open circuit voltage. Furthermore, radiation-induced damage at interfaces has been shown to contribute to performance degradation in thicker devices.¹¹ InAlP and InGaP were selected as n- and p-type passivation layers due to their favorable band alignments, as an alternative to previously employed AlGaAs schemes,²⁶ with a view to obtain good diode characteristics with a fully depleted device design. This has been demonstrated in prior work,²⁸ with the

TABLE I. Ultra-thin device layer structure with nominal doping density and thickness values.

Layer	Material	Dopant	Doping density (cm^{-3})	Thickness (nm)
n-type contact	GaAs	Si	5×10^{18}	300
Hole barrier	$\text{In}_{0.47}\text{AlP}$	Si	5×10^{18}	20
n-type absorber	GaAs	Si	1×10^{17}	40
p-type absorber	GaAs	Be	1×10^{17}	40
Electron barrier	$\text{In}_{0.49}\text{GaP}$	Be	5×10^{18}	20
p-type contact	GaAs	Be	1×10^{19}	25
Etch stop layer	InAlP	Be		150
Substrate	p-GaAs			

difference that the absorber layer doping density was an order of magnitude greater in that study.

To produce on-wafer devices, a mesa etch was carried out to isolate the area of the solar cells. Selective etches removed the layers not protected by resist leaving the p-type contact layer in place. The front annealed n-type contact was evaporated using a lift-off procedure with Ni/AuGe/Ni/Au metallization and 10/135/20/200 nm layer thicknesses. This contact was then annealed for 20 s at 350 °C. The non-annealed p-type contact was then evaporated using the same lift-off procedure with Ti/Au metallization and 20/200 nm layer thicknesses. Finally, the 300 nm n-type GaAs contact layer was removed using selective etch and a resist to protect the areas around the device.

To produce off-wafer devices, an n-type grid contact with 3% coverage was evaporated using a lift-off procedure. This contact was deposited using the same metallisation and anneal settings as for the on-wafer devices. The 300 nm GaAs n-type contact layer was etched away. 450 nm of Ag was then thermally evaporated. The sample was then bonded to a Si carrier chip using a OPT5054-4G two-part Optitec epoxy with a high glassing temperature. The epoxy was cured on a hot plate for 30 min at 120 °C. The GaAs

growth substrate was then etched away with an $\text{NH}_4\text{OH}:\text{H}_2\text{O}_2$ etchant at a ratio of 1:10. The 150 nm InAlP etch stop layer was removed with concentrated HCl. The p-type front contact was evaporated using a lift-off procedure and the same metallisation as the on-wafer devices. The remaining exposed 25 nm GaAs p-type contact layer was etched away. Finally, a mesa etch was carried out to isolate the device areas. Selective etches were used to remove each layer until the Ag was reached.

The on-wafer device is an n-on-p design while the off-wafer device is p-on-n because of the inversion that takes place during adhesive bonding and growth substrate removal. All devices are $2.5 \times 2.5 \text{ mm}^2$ without anti-reflection coatings. On-wafer devices have 10% front contact shading and the off-wafer devices have an improved front contacting scheme with 4.2% shading. Figure 2 shows the layer structure and contact metallization for on- and off-wafer devices.

B. Irradiations

3 MeV proton irradiations took place at the Dalton Cumbrian Facility. A 5 MV tandem pelletron ion accelerator (NEC model 15SDH-4 with a TORVIS source) produced the proton beam. Three identical sets of devices were irradiated to different proton fluences over three separate irradiation sessions. This allowed the variation of material and device parameters with fluence to be studied over a wide range of fluences, from 3×10^{11} to $3 \times 10^{15} \text{ cm}^{-2}$. It was necessary to adjust the beam flux depending on the target fluence due to time constraints. The beam flux used ranged from 2×10^{10} to $3 \times 10^{11} \text{ cm}^{-2} \text{ s}^{-1}$, though it was kept constant during any single irradiation.

During irradiations with fluences below $1 \times 10^{15} \text{ cm}^{-2}$, the temperature of the samples did not increase significantly above room temperature. However, for fluences of $1 \times 10^{15} \text{ cm}^{-2}$ and above, the higher beam current produced some heating. The maximum temperature reached by the thermocouple spot welded to the aluminium carrier plate was approximately 90 °C, which is

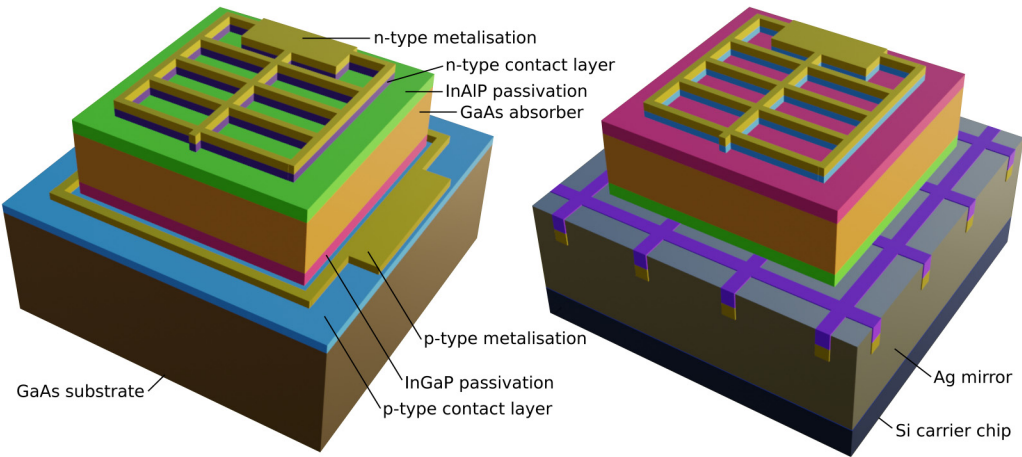


FIG. 2. Diagram of on (left) and off-wafer (right) ultra-thin solar cells; lengths are not to scale.

well below the glassing temperature of the epoxy (only applicable to the off-wafer devices), although the local temperature at the front surface of the devices could be significantly higher.

C. Cathodoluminescence

Cathodoluminescence imaging is a scanning electron microscopy-based technique.³¹ The incident electrons interact with the target material through different mechanisms. One of these is inelastic scattering from valence band electrons, which imparts some energy to them and excites them to the conduction band, i.e., electron-hole pair creation. Cathodoluminescence is observed if these carriers recombine radiatively. This luminescence can then be resolved spectrally, spatially, and temporally to study a variety of material properties. Being an electron microscope-based technique, a high spatial resolution can be achieved. This allows direct observation of radiation-induced non-radiative defects in the absorber layer of the UTSCs.

In this study, an Attolight Allalin 4027 Chronos TRCL system has been employed. The time-resolved capabilities are enabled by producing a pulsed electron beam through the photoelectric effect using a pulsed laser focused on a cold electron gun.³² A Hamamatsu streak camera was used for time-resolved detection^{32,33} and a Si CCD was used for detection in continuous wave mode.

D. Device characterization

Dark IV sweeps were carried out using a Keithley 2401 SMU at room temperature in complete darkness. A two-diode model³⁴ was fit to the data to extract diode characteristics (reverse bias saturation currents J_{01} and J_{02} , series resistance R_{ser} , and parallel resistance R_{par}),

$$J = J_{01} \exp \left[\frac{q(V - JR_{ser})}{n_1 kT} \right] + J_{02} \exp \left[\frac{q(V - JR_{ser})}{n_2 kT} \right] + \frac{V - JR_{ser}}{R_{par}}. \quad (1)$$

The diode one ideality factor was fixed at $n_1 = 1$, while the diode two ideality factor (n_2) was a free parameter.

Light IV was performed with a dual-source TS Space Systems Compact Solar Simulator using an AM0 spectrum. Calibration was carried out with a spectrophotometer. A water-cooled system maintained test temperature at 25°C.

III. RESULTS

A. Cathodoluminescence

Cathodoluminescence was performed on on-wafer orientation of the UTSCs, and an electron beam energy of 5 keV was used to directly excite the entire absorber layer. 90% of the beam energy is deposited in an interaction volume with a depth of ~130 nm and a width of ~140 nm according to Monte Carlo simulations.³⁵ This means that we expect some generation of electron hole pairs in the p++ GaAs buffer, which was not found to contribute significantly to the luminescence emanating from the sample. The beam current used when operating in continuous wave mode was 5 ± 0.5 nA. The average current of the pulsed beam used in time-resolved mode was 100 ± 10 pA.

Figures 3(a)–3(f) are a series of integrated CL intensity maps, to which a bandpass filter from 845 to 895 nm has been applied. This spectral band was chosen to select out the main/band-edge GaAs peak. The figure shows the increasing density of non-radiative defects with proton fluence in the absorber layer. The relative brightness of the maps is not indicative of their relative mean intensities, which can instead be seen in the mean spectra in Fig. 3(h). The mean intensity decreases with greater proton fluence, to an extent that would mask the contrast introduced by individual non-radiative defects if the intensity maps were all plotted with the same intensity scale. Figure 3(g) is the secondary electron (SE) image of the exact same area as Fig. 3(f) and it is also representative of the SE images collected in the locations of Figs. 3(a)–3(e). This shows that the dark spots in the CL maps are not related to any surface features and that the surface topography is not affected by irradiation.

The dark spots indicate non-radiative defects,^{16,31,36–38} though the identity of these defects cannot be concluded from this technique. Multiple factors may contribute to variation in dark spot size and darkness. These include defect depth in the absorber layer, defect type, and defect overlap.³⁹

Defect type can have an effect on recombination rate, dependent on the capture cross section and the different energy states introduced into the bandgap by a given defect.⁴⁰ A defect with a higher non-radiative recombination rate will appear darker.^{39,41}

Overlap of defects refers to two phenomena. First, it is important to realize that the dark spots associated with defects in the CL maps are significantly larger than the defects themselves, because carriers can diffuse to the defect from its vicinity. The greater the distance from the defect, the lower the probability that a carrier will be captured, and hence, the intensity increases radially outward from any one defect. Overlap may, therefore, refer to overlap of dark regions, i.e., areas of influence of a defect. It may also refer to defects that are located at the same lateral position but different depths.

The depth of a defect can change how dark it appears as light produced deep in the sample tends to contribute less to the total light detected at any one beam position. Depth is unlikely to have a great effect in these samples, because the absorber layer only extends to a depth of 100 nm. As the interaction volume penetrates to a depth of ~130 nm, significant electron-hole pair generation is expected throughout the entire 80 nm thick absorber layer. Reabsorption of emitted light is expected to be negligible for such a thin absorber layer, as the absorption coefficient of GaAs is still relatively small near the band edge.⁴² The passivation layers prevent carriers from diffusing deeper into the sample. Previous studies^{43–45} have suggested that both point and clusters of point defects are produced by proton irradiation. It is, therefore, possible that the darkness of spots in the CL maps is indicative of defect cluster size.

A consequence of this variability in spot darkness is that determination of radiation-induced defects over background noise with confidence becomes difficult, preventing precise measurement of the spot density. This is compounded by the overlapping of dark spots of different intensities, which becomes increasingly problematic with increasing fluence.

No shift in peak position or shape was observed with radiation. The peak position at 879 ± 1 nm is red-shifted from what

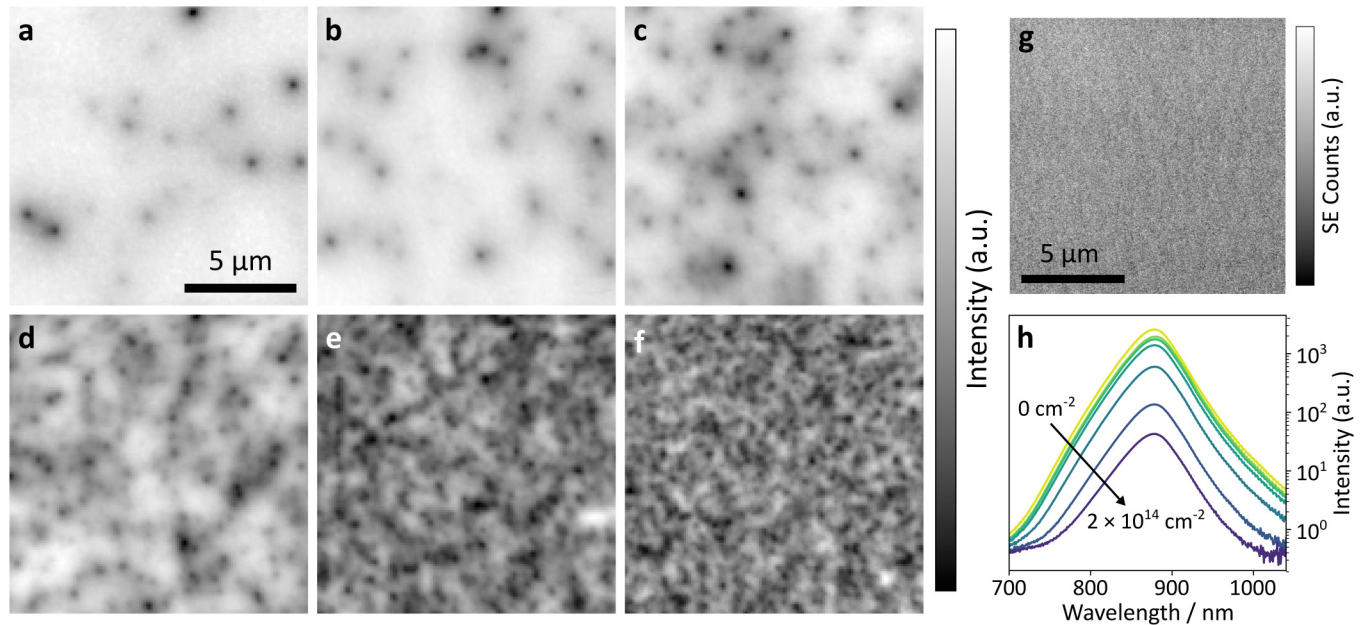


FIG. 3. (a)–(f) Band-pass integrated CL intensity maps, from 845 to 895 nm, for 3 MeV proton-irradiated sample series. Proton fluences are (a) 3×10^{11} , (b) 1×10^{12} , (c) 3×10^{12} , (d) 2×10^{13} , (e) 1×10^{14} , and (f) 2×10^{14} cm⁻². 5 keV beam energy and 5 nA beam current were used. (g) SE image of the planar surface of the 2×10^{14} cm⁻² sample, and the CL map of which is shown in (f). (h) Mean spectra of the CL maps shown in (a)–(f). All CL data were recorded at room temperature, and the scale bar in (a) applies to all CL images.

might be expected for both n- and p-type GaAs with 1×10^{17} cm⁻³ doping at room temperature.⁴⁶ The peak width is also greater than that observed for pure n- and p-type materials with equivalent doping concentrations.⁴⁶ These discrepancies between the luminescence from the absorber layers of the ultra-thin cells and pure n- and p-type materials may be accounted for by the strong built-in field present in the devices. The electric field across the fully depleted absorber layer may enhance sub-bandgap absorption and emission. This is known as the Franz-Keldysh effect and it has already been shown to be of particular relevance in ultra-thin device geometries.^{47,48}

The lack of variation in the peak with radiation is mainly attributed to experimental limitations. The room temperature peak is very broad and the lowest resolution grating available was used to be able to capture the entire peak. The Si-CCD detector IQE drops off sharply in the range of 900–1100 nm, such that variations in the low-energy tail may become obscured by noise. As a result, small variations in peak position and shape are unlikely to be resolved.

Time-resolved data were acquired using a Hamamatsu streak camera. Multiple streak images, in different locations, were taken for each sample. The area sampled for acquisition of any single streak image was $\sim 5 \mu\text{m}$ square. This field of view was taken as a compromise, allowing the acquisition of spatially averaged data, without significantly affecting temporal resolution or the CL intensity coupling into the streak camera. Taking streak images in multiple locations allowed for further spatial averaging. Single

exponentials were then fitted to time traces of integrated intensity to extract carrier lifetime. Intensity was integrated from 850 to 870 nm to give a greater signal to noise ratio. Use of a wide wavelength range was justified as any spectral variation in lifetime observed in this range was negligible relative to the spatial variation in lifetime due to taking streak images at different locations on the sample, which dominated the uncertainty in measured lifetime. The averages of the lifetimes measured at different locations on each sample are plotted against proton fluence in Fig. 4, with the error bars representing the standard deviation in these measurements. The inset shows an example of a time trace—only the falling edge is shown for clarity—for each sample, normalized to the respective peak intensities. The full, normalized time traces along with the instrument response function and a fit to the 2×10^{14} cm⁻² time trace are given in the [supplementary material](#).

CL data for samples irradiated to fluences greater than 2×10^{14} cm⁻² are not included because carrier lifetime for these samples is below the instrument response time and cannot be extracted.

Minority carrier lifetime, τ , is expected to vary with fluence, Φ , as

$$\frac{1}{\tau} = \frac{1}{\tau_0} + K_{\tau}\Phi, \quad (2)$$

where K_{τ} is the lifetime damage constant and τ_0 is the pre-irradiation lifetime. The data were fit using this relationship,

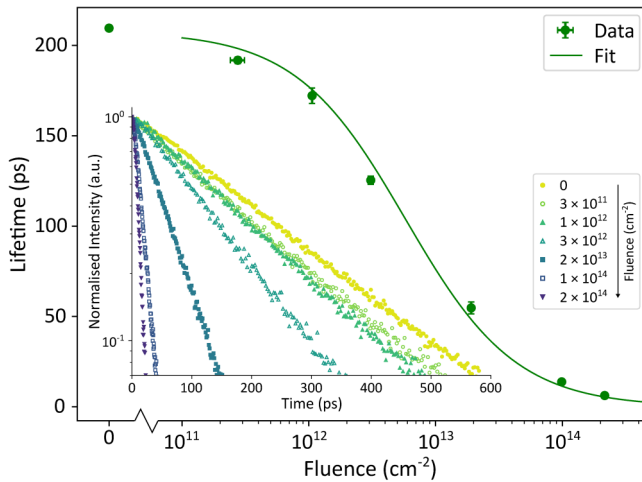


FIG. 4. Minority carrier lifetime, extracted from CL time traces is plotted against fluence. The fit to the data is also shown. The inset shows the trailing edges of the time traces, which were fitted with single exponential decays to extract the lifetimes.

yielding $K_r = (8.3 \pm 0.9) \times 10^{-4} \text{ cm}^2 \text{ s}^{-1}$ and $\tau_0 = 208 \pm 3 \text{ ps}$. The fit is in good agreement with the experimental data.

The initial lifetime is low for GaAs, likely due to the spatial confinement of the carriers in the ultra-thin absorber layer. This gives greater wavefunction overlap between electrons and holes than would be found in bulk GaAs and, therefore, greater recombination rate and lower lifetime.⁴⁹ The lifetime decreases with fluence for the same reason that continuous wave CL intensity drops with fluence.³¹ As more non-radiative defects are introduced by radiation, the non-radiative recombination rate of carriers increases, such that the lifetime of carriers decreases.

By using non-ionizing energy loss theory (NIEL),⁵⁰ K_r can be expressed relative to displacement damage dose, giving $K_{r, \text{DDD}} = (4.3 \pm 0.4) \times 10^{-2} \text{ g MeV}^{-1} \text{ s}^{-1}$. This is in agreement with previously reported values, which range from 1.2×10^{-2} to $52 \times 10^{-2} \text{ g MeV}^{-1} \text{ s}^{-1}$.^{10,11,51–53}

B. Device performance

On- and off-wafer UTSCs were electrically characterized before and after irradiation with 3 MeV protons. The results of this characterization are shown in Fig. 5. The on-wafer devices show a significant improvement in maximum power (P_{max}) at all fluences over previous on-wafer 80 nm devices reported by Hirst *et al.*,²⁶ with greater open-circuit voltage (V_{oc}) and lower J_{02} primarily attributed to the improvement in passivation layers. The off-wafer devices show a further increase in short-circuit current (J_{sc}) due to the introduction of the Ag back surface mirror and the resulting double-pass absorption. Data from three other single-junction GaAs solar cells with a variety of absorber layer thicknesses are also plotted as a comparison. The data from the 3500 nm cells⁵⁴ were originally taken with 2 MeV protons so they were scaled to 3 MeV equivalent fluences using the displacement damage dose method.⁵⁰

The UTSCs show no degradation in short circuit current [Fig. 5(a)] up to extremely high fluences (10^{15} cm^{-2}) while the open circuit voltage degradation [Fig. 5(b)] occurs at a similar rate for all device thicknesses and across all fluences studied here. These effects result in the off-wafer UTSC P_{max} exceeding that of much thicker devices, even at relatively modest fluences ($< 10^{12} \text{ cm}^{-2}$).

At fluences $> 10^{15} \text{ cm}^{-2}$, a collapse in J_{sc} is observed in the on-wafer UTSC (see Discussion section A). While data from only one series of on-wafer devices are shown in Fig. 5, the same behavior was observed in a second, nominally identical series of devices (see supplementary material). Electrical characterization of off-wafer devices could not be performed at these highest fluences because of sample damage occurring during exposure. Higher beam currents were required for the highest fluences, which resulted in visible damage to the off-wafer devices, where the film started to delaminate from the carrier. This may be due to the mismatch in the thermal expansion coefficient between the epoxy and device layers. It may also be the result of localized heating, beyond that detected on the thermocouple, due to restricted thermal diffusion through the epoxy layer. While the effects of localized sample heating due to accelerated damage testing are artificial and not demonstrative of real space environments, space photovoltaics will experience thermal cycling. These observations highlight the relative fragility of off-wafer embodiments to such effects, motivating further study.

Figure 5(d) shows the J_{02} values, extracted from fitting a two-diode model to dark IV data. Linear lines of best fit were added to the log-log plot to compare the trend in J_{02} degradation between different device types. The trend for all devices is similar, with the gradients of the lines being close to 1 (see Discussion section B).

IV. DISCUSSION

A. Collapse of short-circuit current

The limit of the ultra-thin design's radiation tolerance is observed as a sharp drop off in J_{sc} past a proton fluence of 10^{15} cm^{-2} in Fig. 5(a). The minority carrier lifetime in this fluence range can be obtained by extrapolating the fit (Eq. 2) to the lifetime against fluence data from Fig. 4. This gives a carrier lifetime of 1–0.1 ps for the fluence range $1 \times 10^{15} - 1 \times 10^{16} \text{ cm}^{-2}$. This is compared with the time required for carriers to traverse the 80 nm thick junction. The junction is fully depleted, and as such, the motion of carriers is dominated by the electric field across the junction. The “traverse time” can, therefore, be calculated from the drift velocity, which is proportional to the carrier mobility and electric field. Since the junction is fully depleted, with the depletion region extending into the passivation layers, which have a significantly greater doping concentration than the absorber layer, the electric field can be approximated to be constant across the junction, with the entire potential drop occurring over the width of the junction, $\sim 80 \text{ nm}$. With these assumptions, the following equation for traverse time, t_{tr} , is found,

$$t_{\text{tr}} = \frac{W^2}{\mu V}, \quad (3)$$

where W is the junction width, μ is carrier mobility, and V is the built-in voltage across the junction. Holes have a lower mobility than

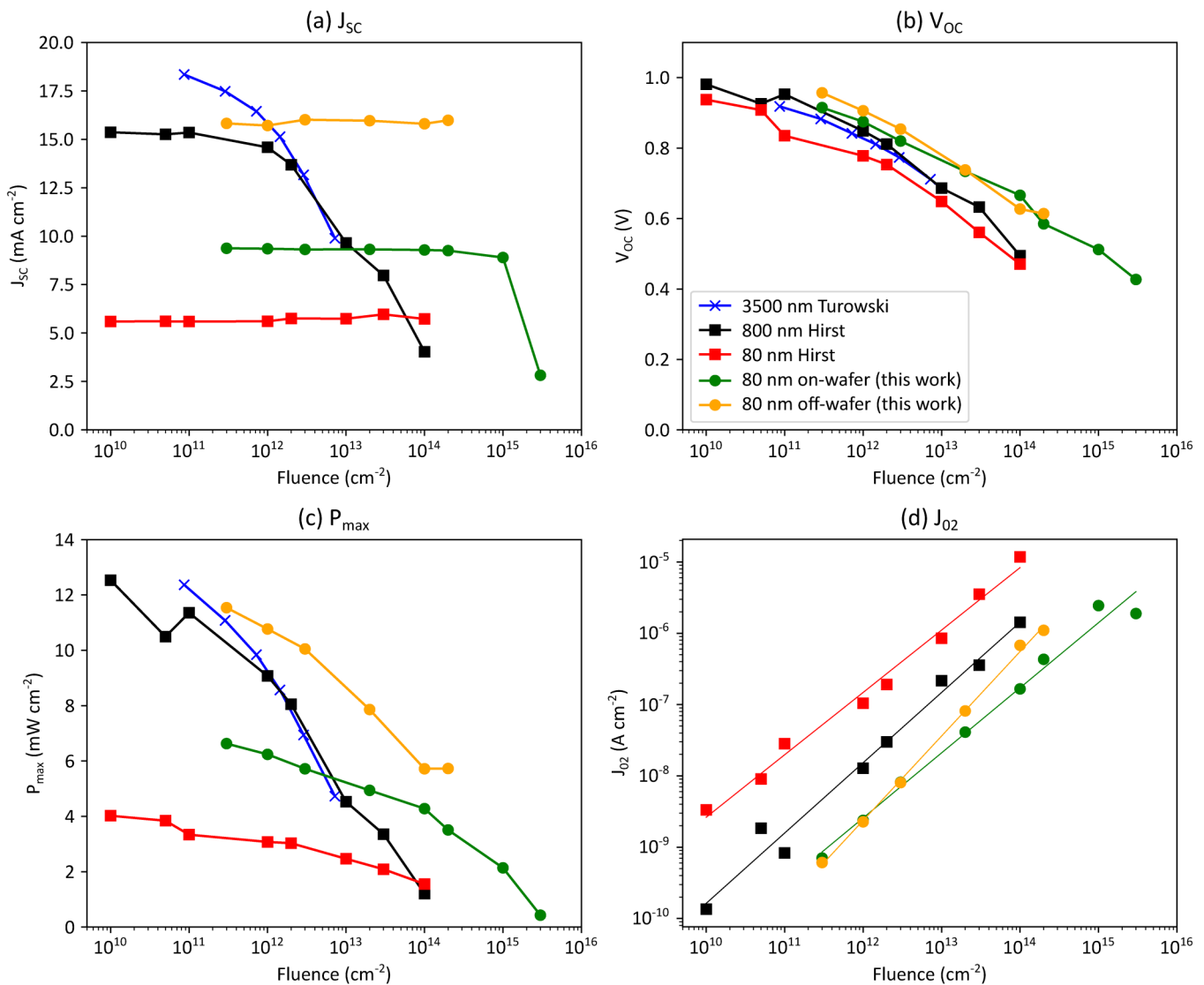


FIG. 5. Absolute values of (a) short-circuit current, (b) open-circuit voltage, (c) maximum power, and (d) J_{02} of 5 different device types as a function of 3 MeV proton equivalent fluence. Connecting lines are used between data points for (a), (b), and (c) purely as a visual guide and linear lines of best fit are used for (d).

electrons in GaAs and will, therefore, have the greater traverse time and be the limiting factor. Using a hole mobility of $490 \text{ cm}^2 \text{ V}^{-1} \text{ s}^{-1}$,⁵⁵ a hole traverse time of $\sim 0.1 \text{ ps}$ is calculated. This hole traverse time is on the same order of magnitude as the extrapolated carrier lifetime in the $1 \times 10^{15} - 1 \times 10^{16} \text{ cm}^{-2}$ fluence range, given above. This result shows that the sharp decrease in short-circuit current coincides with the point at which carrier lifetime and traverse time become comparable, which means that the fraction of carriers that recombine before reaching the passivation layers increases drastically in this range. It is important to note that the value for traverse time calculated here is a lower bound, since mobility is likely to be degraded by radiation^{56–58} and the built-in voltage will likely decrease

due to compensation from the introduction of majority carrier traps by radiation.^{37,54,59} Taking drift velocity saturation⁶⁰ into account would also yield a greater traverse time, though the increase would be less than an order of magnitude. The effect of drift velocity saturation would also be diminished by the previous two factors, as well as saturation velocity overshoot, which may be a significant effect at these short time scales.^{61,62}

B. Analysis of current-voltage behaviour

Figure 6 shows the DIV curves of the on-wafer UTSCs with increasing proton fluence. The two-diode model given in

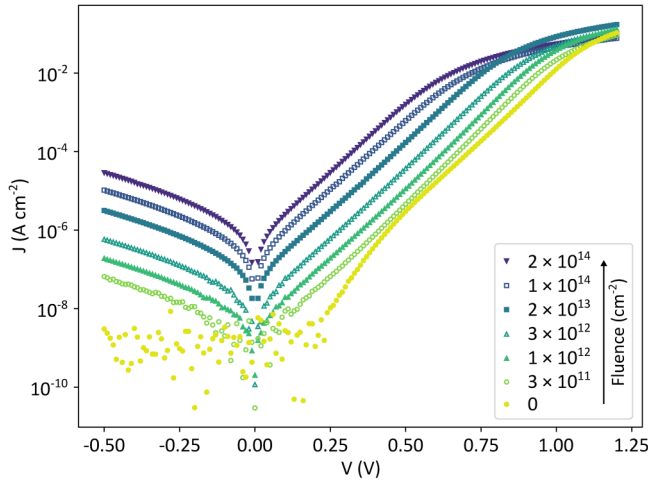


FIG. 6. Dark I-V curves for the sample series, including irradiated and unirradiated devices, are shown.

Experimental Methods section D was used to extract diode parameters from this data set (Table II). It was found that the second diode dominates over the first diode for the entire voltage range measured, which is expected as these devices will be fully depleted at zero bias and under low forward bias. Recombination in the depletion region is expected to be predominantly trap-assisted bimolecular, which would be described by a second diode with an ideality factor $n_2 = 2$.⁶³ However, after irradiation, values of $n_2 > 2$ are extracted. This increase in n_2 after irradiation may be indicative of a different dominant recombination process. As n_2 does not vary greatly between 3×10^{11} and $2 \times 10^{14} \text{ cm}^{-2}$, the values of the second diode reverse saturation current, J_{02} , should be comparable in this range.

J_{02} is the dominant parameter quantifying the current-voltage characteristics of these devices. J_{02} is plotted as a function of both fluence and inverse Shockley-Read-Hall (SRH) carrier lifetime, together with respective directly proportional fits in Fig. 7. The fits are in good agreement with the data, as is expected for a fully depleted device in which recombination is dominated by a trap-assisted mechanism with a single deep-level trap.²⁶

TABLE II. 2-diode model fitting results for on-wafer devices.

Fluence (cm^{-2})	J_{02} (A cm^{-2})	n_2	R_{ser} ($\Omega \text{ cm}^2$)
Pre-exposure	1.16×10^{-10}	2.05	1.29
3×10^{11}	7.03×10^{-10}	2.21	2.26
1×10^{12}	2.38×10^{-9}	2.28	1.84
3×10^{12}	8.14×10^{-9}	2.30	2.29
2×10^{13}	4.11×10^{-8}	2.33	2.04
1×10^{14}	1.66×10^{-7}	2.35	5.75
2×10^{14}	4.31×10^{-7}	2.33	5.53
1×10^{15}	2.44×10^{-6}	2.71	4.10
3×10^{15}	1.89×10^{-6}	2.80	7.16

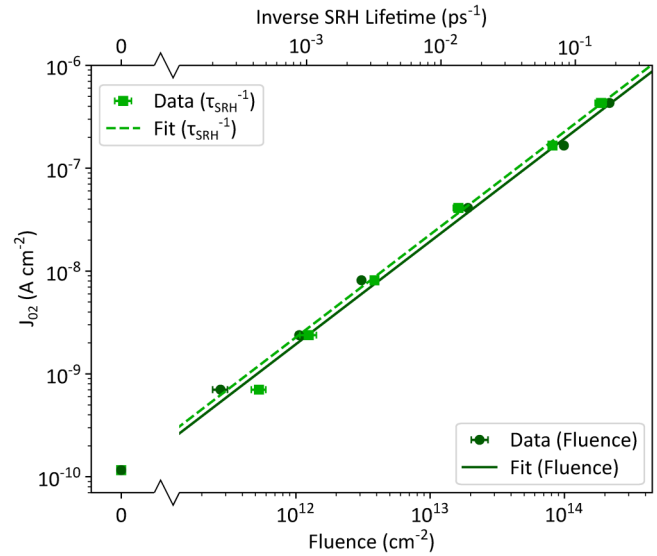


FIG. 7. The variation of J_{02} with fluence and inverse Shockley-Read-Hall (SRH) carrier lifetime (τ_{SRH}^{-1}) is shown with logarithmic axes. Directly proportional fits to both sets of data are also plotted. The inverse SRH lifetime axis has been scaled using the lifetime damage constant, K_r , obtained from fitting lifetime against fluence data (see Fig. 4). This correlates the values of inverse SRH lifetime with fluence. Each data point corresponds to a single sample. The lower fluence data points have larger uncertainties due to the shorter irradiation time.

The inverse proportionality between J_{02} and SRH lifetime in the space charge region (SCR), $\tau_{\text{SRH,SCR}}$, is given by Sah *et al.*,⁶³

$$J_{02} = \frac{qWn_i}{2\tau_{\text{SRH,SCR}}}. \quad (4)$$

Here, q is the elemental charge, W is the junction width, and n_i is the intrinsic carrier concentration.

The SRH lifetimes of the samples in this study can be extracted from the carrier lifetimes measured via TRCL. This is done using Matthiessen's rule [Eq. (5)], assuming that the TRCL lifetime represents the total carrier lifetime (τ_{total}), that SRH recombination is the dominant non-radiative recombination mechanism and that radiative recombination dominates in the unirradiated sample,⁶⁴ such that the TRCL lifetime of this sample (τ_0) is approximately equal to the radiative lifetime (τ_r) in all of the samples,

$$\frac{1}{\tau_{\text{total}}} = \frac{1}{\tau_r} + \frac{1}{\tau_{\text{SRH}}}. \quad (5)$$

By applying these assumptions and substituting Eq. (2) into Eq. (5), it is found that the SRH lifetime in these cells is inversely proportional to fluence,

$$\frac{1}{\tau_{\text{SRH}}} = K_r \Phi. \quad (6)$$

The substitution of Eq. (6) into Eq. (4) yields the directly proportional relationship between J_{02} and fluence,

$$J_{02} = \frac{qWn_i}{2} K_r \Phi. \quad (7)$$

A comparison of Eqs. (4) and (7) shows that the respective proportionality constants, correlating J_{02} with inverse SRH lifetime, $k(J_{02}, \tau_{\text{SRH}}^{-1})$, and fluence, $k(J_{02}, \Phi)$ should differ by a factor of K_r . Therefore, taking the ratio of these constants provides an alternative measure of the lifetime damage constant. Values of the proportionality constants are obtained by calculating the gradients of the lines of fit in Fig. 7, giving $k(J_{02}, \tau_{\text{SRH}}^{-1}) = (2.73 \pm 0.05) \times 10^{-18} \text{ A cm}^{-2} \text{ s}$ and $k(J_{02}, \Phi) = (1.94 \pm 0.05) \times 10^{-21} \text{ A}$. The ratio of these gives $K_r = (7.1 \pm 0.2) \times 10^{-4} \text{ cm}^2 \text{ s}^{-1}$, which is very close to the value of $(8.3 \pm 0.9) \times 10^{-4} \text{ cm}^2 \text{ s}^{-1}$ extracted from the plot of lifetime against fluence (see Fig. 4). The small difference in these values is represented by the slight shift between the lines of fit in Fig. 7, since the inverse SRH lifetime axis has been scaled according to Eq. (6), using the value of K_r from Fig. 4. This result shows that, for these devices, the assumptions leading to Eqs. (6) and (7) are justified and that the recombination statistics follow a SRH deep-level trap model.

Furthermore, a value for the intrinsic carrier lifetime of GaAs can be calculated from $k(J_{02}, \tau_{\text{SRH}}^{-1})$, using Eq. (4) and assuming a depletion region width of 80 nm, yielding $n_i = (4.26 \pm 0.08) \times 10^6 \text{ cm}^{-3}$. This is close to the room temperature value found by other authors.⁶⁵ This provides further evidence that the SRH single deep-level trap model and resulting Eq. (4) are applicable to these devices.

However, some adjustment to the model is required to account for the deviation of n_2 from its expected value post-irradiation. It has already been shown that adjustments to the SRH deep-level trap model are required to account for variations in the local ideality factor, $n(V)$, although these studies focus on thicker devices where $n(V)$ is found to vary in the range $1 < n(V) < 2$.^{56,67}

It may be possible to explain this partial SRH behavior by considering the introduction of defect clusters. Through interaction between neighboring defects, the current-voltage behavior may be augmented to give $n_2 > 2$.^{68–70} However, as clusters are introduced by single collision events, that are spatially separated, it is not unexpected that J_{02} remains proportional to inverse lifetime and fluence. This relationship would only be expected to break down at sufficiently high fluences, where overlap of clusters becomes frequent. The effects described above are not observed in radiation degradation studies of thicker cells.²⁶ It may be that thicker cells are not dominated by depletion region recombination and defect clusters are likely to behave differently in depletion and quasi-neutral regions, being affected by the presence of an electric field.

A different explanation is offered by considering a trap-assisted tunnelling mechanism, which is facilitated by the strong electric field across the absorber layer in these devices. This effect has been shown to account for high ideality factor in InGaN/GaN multiple quantum well light-emitting diodes^{71–73} and has been predicted to result in values of n that are slightly greater than 2 in ultra-thin solar cells.⁷⁴ The effect results in an elevated value of n , because the trap-assisted tunnelling provides an addition to the recombination current, which diminishes with increasing

forward bias, since this reduces the electric field across the junction and hence the tunnelling probability.

While a fully theoretical explanation for the behavior of the devices remains elusive, the agreement in observations of this study with those of Hirst *et al.*²⁶ is of significant importance. It demonstrates that the J_{02} of UTSCs can be expected to be proportional to proton fluence, as in conventional cells, despite being fully depleted. Furthermore, the ideality factor of fully or mostly depleted UTSCs after proton irradiation can be expected to exceed 2.

C. Implications for space power systems

The advantage of the high radiation tolerance of UTSCs is highlighted by considering the potential savings on cover glass mass, in comparison to a thicker cell. In Fig. 8, the P_{max} remaining factor is plotted against CMG⁷⁵ cover glass thickness for the on and off-wafer UTSCs and the previously reported 80 and 800 nm cells from Hirst *et al.*²⁶ in a Molniya orbit for 20 years. This figure was generated by combining the data from Fig. 5(c) with simulated data for the variation of non-ionizing dose at the absorber layer with CMG cover glass thickness. The simulation was carried out using MULASSIS⁷⁶ and SPENVIS.¹² AP-9/AE-9 mean fluxes were used and single event upsets were not considered.

The plot demonstrates that for the 80 nm devices from this work, a significantly thinner layer of cover glass than for the 800 nm Hirst cell will result in the same P_{max} . For example, for the 80 nm off-wafer and 800 nm cells to both end up with a P_{max} of 7 mW cm^{-2} , after 20 years on Molniya orbit, the 80 nm cell requires ~ 3.2 times less cover glass. This would correspond to a significant reduction in solar array mass and, therefore, launch cost for a satellite using such an array.

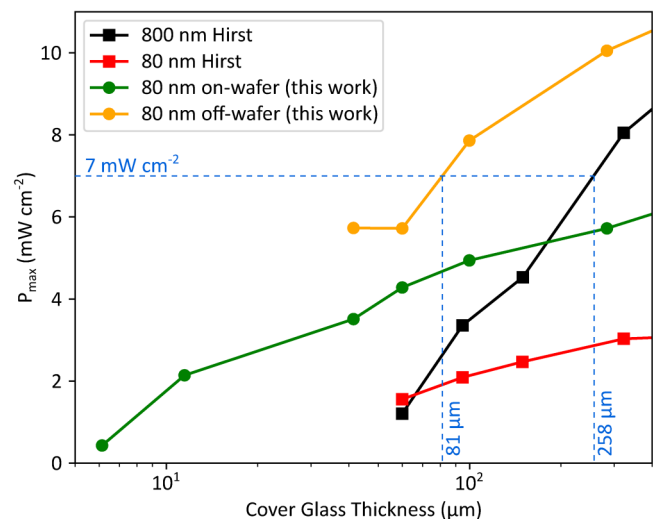


FIG. 8. The variation of P_{max} for various device types with CMG cover glass thickness after 20 years on a Molniya orbit is shown. Connecting lines are used between data points purely as a visual guide. The blue dashed lines highlight that the off-wafer cell requires less shielding from cover glass than the 800 nm Hirst cell (81 μm and 258 μm , respectively) to provide the same P_{max} (7 mW cm^{-2}).

V. CONCLUSIONS

It has previously been shown that 80 nm GaAs solar cells do not exhibit J_{sc} degradation upon exposure to 3 MeV proton fluence up to 10^{14} cm^{-2} . In this work, the inherent radiation resilience of this geometry is demonstrated in devices with enhanced P_{max} , achieved by (i) reducing depletion region recombination, as characterized by a reduction in reverse bias saturation current J_{02} and (ii) increasing J_{sc} by removing the growth substrate and integrating a rear surface Ag mirror for light management. The improved UTSC outperforms the previously studied thicker devices, for 3 MeV proton fluences $> 10^{12} \text{ cm}^{-2}$, lowering the fluence threshold, over which ultra-thin geometries offer favorable performance, by two orders magnitude relative to previous observations.

The underlying mechanisms that are responsible for radiation resilience in UTSCs are further elucidated through characterization with time-resolved cathodoluminescence. Using this technique, radiation-induced defects are mapped with increasing 3 MeV proton fluence. A reduction in the bandgap luminescence peak intensity of ~ 2 orders of magnitude is observed, along with a reduction in minority carrier lifetime from $208 \pm 3 \text{ ps}$ pre-radiation to $6.2 \pm 0.6 \text{ ps}$, after exposure to $2 \times 10^{14} \text{ cm}^{-2}$ fluence. Despite this substantial reduction in luminescence and minority carrier lifetime, device J_{sc} remains unchanged, until fluence reaches 10^{15} cm^{-2} , beyond which it collapses. At this extreme damage level, minority carrier lifetime can no longer be directly measured but is extrapolated to be 1–0.1 ps in the fluence range of $1 \times 10^{15} - 1 \times 10^{16} \text{ cm}^{-2}$, consistent with the calculated time taken for holes to traverse the ultra-thin film. By pushing the radiation resilience of UTSCs to the point of failure, it is corroborated that this effect derives from the minority carrier lifetime remaining longer than the time taken by carriers to travel the short distance to the device terminals. Once this condition is breached, J_{sc} collapses. The nature of radiation-induced defects is further studied by extracting diode parameters as a function of fluence. The directly proportional relationships between J_{02} , inverse SRH lifetime, and fluence, with self-consistent proportionality constants, indicate that the recombination statistics are similar to a simple SRH single deep-level trap model; however, values of $n_2 > 2$ suggest that bimolecular recombination does not fully describe the observed behavior. It is proposed that ultra-thin cells, due to their fully depleted design, may be sensitive to the presence of defect clusters and to trap-assisted tunnelling.

The implication of this work for space power systems is that the high radiation tolerance of the UTSCs displayed will enable a significant reduction in cover glass mass required for radiation-shielding solar arrays on orbit. It was shown that the off-wafer cells from this work would require ~ 3.2 times less cover glass than previously reported thicker 800 nm cells to deliver the same P_{max} of 7 mW cm^{-2} after 20 years in a Molniya orbit. This reduction in solar array mass translates to an overall lighter space power system with lower launch costs.

SUPPLEMENTARY MATERIAL

See the [supplementary material](#) for figures showing the full, normalized CL time traces, of which only the trailing edges are shown in the inset of Fig. 4. These figures also show the TRCL

instrument response function and a fit to the $2 \times 10^{14} \text{ cm}^{-2}$ time trace. A figure showing the variation of J_{sc} with fluence for both series of on-wafer devices, the first of which is shown in Fig. 5(a), is also included.

ACKNOWLEDGMENTS

We acknowledge the support of The University of Manchester's Dalton Cumbrian Facility (DCF), a partner in the National Nuclear User Facility, the EPSRC UK National Ion Beam Centre and the Henry Royce Institute. We recognize Carl Andrews for their assistance during irradiations.

Financial support for the CL equipment and measurements was provided by the EPSRC under No. EP/R025193/1.

This work was further supported by the H2020 European Research Council under No. 853365 and the UK Space Agency under No. PF2-012.

A. Barthel acknowledges support from his EPSRC PhD Studentship, EP/R513180/1.

AUTHOR DECLARATIONS

Conflict of Interest

The authors have no conflicts to disclose.

Author Contributions

A. Barthel: Conceptualization (equal); Formal analysis (equal); Investigation (equal); Methodology (equal); Visualization (equal); Writing – original draft (lead); Writing – review & editing (equal). **L. Sayre:** Conceptualization (equal); Formal analysis (equal); Investigation (equal); Methodology (equal); Visualization (equal); Writing – original draft (equal); Writing – review & editing (equal). **G. Kusch:** Formal analysis (supporting); Methodology (equal); Resources (equal); Supervision (equal); Writing – review & editing (supporting). **R. A. Oliver:** Funding acquisition (equal); Resources (equal); Writing – review & editing (supporting). **L. C. Hirst:** Conceptualization (equal); Funding acquisition (lead); Project administration (lead); Resources (equal); Supervision (lead); Writing – original draft (supporting); Writing – review & editing (equal).

DATA AVAILABILITY

The data that support the findings of this study are available from the corresponding author upon reasonable request.

REFERENCES

- ¹D. Hastings and H. Garrett, *Spacecraft-Environment Interactions* (Cambridge University Press, Cambridge, 1996).
- ²Y. Zheng, N. Y. Ganushkina, P. Jiggins, I. Jun, M. Meier, J. I. Minow, T. P. O'Brien, D. Pitchford, Y. Shprits, W. K. Tobiska, M. A. Xapsos, T. B. Guild, J. E. Mazur, and M. M. Kuznetsova, "Space radiation and plasma effects on satellites and aviation: Quantities and metrics for tracking performance of space weather environment models," *Space Weather* **17**, 1384–1403 (2019).
- ³Y. Lu, Q. Shao, H. Yue, and F. Yang, "A review of the space environment effects on spacecraft in different orbits," *IEEE Access* **7**, 93473–93488 (2019).

- ⁴H. Y. Tada, J. R. J. Carter, B. E. Anspaugh, and R. G. Downing, *Solar Cell Radiation Handbook*, 3rd ed. (Jet Propulsion Laboratory, California Institute of Technology, Pasadena, CA, 1982).
- ⁵J. M. Raya-Armenta, N. Bazmohammadi, J. C. Vasquez, and J. M. Guerrero, "A short review of radiation-induced degradation of III–V photovoltaic cells for space applications," *Solar Energy Mater. Solar Cells* **233**, 111379 (2021).
- ⁶J. Li, A. Aierken, Y. Liu, Y. Zhuang, X. Yang, J. H. Mo, R. K. Fan, Q. Y. Chen, S. Y. Zhang, Y. M. Huang, and Q. Zhang, "A brief review of high efficiency III–V solar cells for space application," *Front. Phys.* **8**, 631925 (2021).
- ⁷R. J. Walters, S. R. Messenger, H. L. Cotal, M. A. Xapsos, S. J. Wojtczuk, H. B. Serreze, and G. P. Summers, "Radiation response of heteroepitaxial n+p InP/Si solar cells," *J. Appl. Phys.* **82**, 2164–2175 (1997).
- ⁸G. P. Summers, R. J. Walters, S. R. Messenger, and E. A. Burke, "Role of radiation-hard solar cells in minimizing the costs of global satellite communication systems," *Prog. Photovolt. Res. Appl.* **4**, 147–154 (1996).
- ⁹K. Nordlund, S. J. Zinkle, A. E. Sand, F. Granberg, R. S. Averback, R. E. Stoller, T. Suzudo, L. Malerba, F. Banhart, W. J. Weber, F. Willaime, S. L. Dudarev, and D. Simeone, "Primary radiation damage: A review of current understanding and models," *J. Nucl. Mater.* **512**, 450–479 (2018).
- ¹⁰S. Khanna, S. Charbonneau, P. Piva, M. Parenteau, and C. Carlone, "Effects of 3 MeV proton irradiation on the excitonic lifetime in gallium arsenide," *IEEE Trans. Nucl. Sci.* **45**, 2430–2435 (1998).
- ¹¹N. Gruginskie, F. Cappelluti, M. van Eerden, G. Bauhuis, P. Mulder, E. Vlieg, and J. Schermer, "Proton irradiation induced GaAs solar cell performance degradation simulations using a physics-based model," *Solar Energy Mater. Solar Cells* **223**, 110971 (2021).
- ¹²D. Heynderickx, B. Quaghebeur, J. Wera, E. J. Daly, and H. R. D. Evans, "New radiation environment and effects models in the European Space Agency's space Environment Information System (SPENVIS)," *Space Weather* **2**, S10S03 (2004).
- ¹³S. Q. Kidder and T. H. Vonder Haar, "On the use of satellites in molniya orbits for meteorological observations of middle and high latitudes," *J. Atmos. Ocean. Technol.* **7**, 517–522 (1990).
- ¹⁴A. P. Trishchenko and L. Garand, "Spatial and temporal sampling of polar regions from two-satellite system on molniya orbit," *J. Atmos. Oceanic Technol.* **28**, 977–992 (2011).
- ¹⁵S. G. Bailey and D. J. Flood, "Space photovoltaics," *Prog. Photovolt. Res. Appl.* **6**, 1–14 (1998).
- ¹⁶A. Barthel, L. Sayre, F. Lang, G. Kusch, J. Bundesmann, A. Denker, R. Oliver, and L. Hirst, "Cathodoluminescence Study of 68 MeV Proton-Irradiated Ultra-Thin GaAs Solar Cells," in *2020 47th IEEE Photovoltaic Specialists Conference (PVSC)* (IEEE, Calgary, AB, Canada, 2020), pp. 1070–1074.
- ¹⁷A. P. Trishchenko and L. Garand, "Observing polar regions from space: Advantages of a satellite system on a highly elliptical orbit versus a constellation of low earth polar orbiters," *Can. J. Remote. Sens.* **38**, 12–24 (2012).
- ¹⁸D. J. Kessler and B. G. Cour-Palais, "Collision frequency of artificial satellites: The creation of a debris belt," *J. Geophys. Res.: Space. Phys.* **83**, 2637–2646, <https://doi.org/10.1029/JA083iA06p02637> (1978).
- ¹⁹J. Drmola and T. Hubik, "Kessler syndrome: System dynamics model," *Space Policy* **44–45**, 29–39 (2018).
- ²⁰See [Directory.eoportal.org](https://directory.eoportal.org) for "Starlink—eoPortal Directory—Satellite Missions" (2020).
- ²¹S. Campagnola, B. B. Buffington, T. Lam, A. E. Petropoulos, and E. Pellegrini, "Tour design techniques for the Europa clipper mission," *J. Guidance, Control, Dyn.* **42**, 2615–2626 (2019).
- ²²T. Bayer, B. Cooke, I. Gontijo, and K. Kirby, "Europa Clipper mission: the habitability of an icy moon," in *2015 IEEE Aerospace Conference* (IEEE, Big Sky, MT, 2015), pp. 1–12.
- ²³R. T. Pappalardo, W. B. McKinnon, and K. K. Khurana, eds., *Europa* (University of Arizona Press, 2017).
- ²⁴N. Z. Vagidov, K. H. Montgomery, G. K. Bradshaw, and D. A. Wilt, "Light trapping structures for radiation hardness enhancement of space solar cells," *Solar Energy Mater. Solar Cells* **182**, 136–141 (2018).
- ²⁵T. Takamoto, M. Kaneiwa, M. Imaizumi, and M. Yamaguchi, "InGaP/GaAs-based multijunction solar cells," *Prog. Photovolt. Res. Appl.* **13**, 495–511 (2005).
- ²⁶L. C. Hirst, M. K. Yakes, J. H. Warner, M. F. Bennett, K. J. Schmieder, R. J. Walters, and P. P. Jenkins, "Intrinsic radiation tolerance of ultra-thin GaAs solar cells," *Appl. Phys. Lett.* **109**, 033908 (2016).
- ²⁷P. Espinet-Gonzalez, E. Barrigón, G. Otnes, G. Vescovi, C. Mann, R. M. France, A. J. Welch, M. S. Hunt, D. Walker, M. D. Kelzenberg, I. Åberg, M. T. Borgström, L. Samuelson, and H. A. Atwater, "Radiation tolerant nanowire array solar cells," *ACS Nano* **13**, 12860–12869 (2019).
- ²⁸L. Sayre, E. Camarillo Abad, P. Pearce, P. Chausse, P. Coulon, P. Shields, A. Johnson, and L. C. Hirst, "Ultra-thin GaAs solar cells with nanophotonic metal-dielectric diffraction gratings fabricated with displacement Talbot lithography," *Prog. Photovolt. Res. Appl.* **30**, 96–108 (2022).
- ²⁹H. Chen, A. Cattoni, R. D. Lépinau, A. W. Walker, O. Höhn, D. Lackner, G. Siefert, M. Faustini, N. Vandamme, J. Goffard, B. Behaghel, C. Dupuis, N. Bardou, F. Dimroth, and S. Collin, "A 19.9%-efficient ultrathin solar cell based on a 205-nm-thick GaAs absorber and a silver nanostructured back mirror," *Nat. Energy* **4**, 1–7 (2019).
- ³⁰L. Sayre, F. Lang, J. Bundesmann, A. Denker, P. Pearce, A. Johnson, and L. Hirst, "Ultra-thin single-junction GaAs solar cells for extreme space environments," in *2020 47th IEEE Photovoltaic Specialists Conference (PVSC)* (IEEE, Calgary, Canada, 2020), pp. 1621–1625.
- ³¹B. G. Yacobi and D. B. Holt, "Cathodoluminescence scanning electron microscopy of semiconductors," *J. Appl. Phys.* **59**, R1–R24 (1986).
- ³²M. Merano, S. Sonderegger, A. Crottini, S. Collin, P. Renucci, E. Pelucchi, A. Malko, M. H. Baier, E. Kapon, B. Deveaud, and J.-D. Ganière, "Probing carrier dynamics in nanostructures by picosecond cathodoluminescence," *Nature* **438**, 479–482 (2005).
- ³³S. Sonderegger, E. Felten, M. Merano, A. Crottini, J. F. Carlin, R. Sachot, B. Deveaud, N. Grandjean, and J. D. Ganière, "High spatial resolution picosecond cathodoluminescence of InGaN quantum wells," *Appl. Phys. Lett.* **89**, 232109 (2006).
- ³⁴S. Suckow, "2/3 diode fit" computer program (2014); available at <https://nanohub.org/resources/14300>.
- ³⁵D. Drouin, A. R. Couture, D. Joly, X. Tastet, V. Aimez, and R. Gauvin, "CASINO V2. 42—a fast and easy-to-use modeling tool for scanning electron microscopy and microanalysis users," *Scanning* **29**, 92–101 (2007).
- ³⁶W. Liu, J.-F. Carlin, N. Grandjean, B. Deveaud, and G. Jacopin, "Exciton dynamics at a single dislocation in GaN probed by picosecond time-resolved cathodoluminescence," *Appl. Phys. Lett.* **109**, 042101 (2016).
- ³⁷S. I. Maximenko, S. R. Messenger, C. D. Cress, J. A. Freitas, and R. J. Walters, "Application of CL/EBIC-SEM techniques for characterization of radiation effects in multijunction solar cells," *IEEE Trans. Nucl. Sci.* **57**, 5658019 (2010).
- ³⁸T. F. K. Weatherley, W. Liu, V. Osokin, D. T. L. Alexander, R. A. Taylor, J.-F. Carlin, R. Butté, and N. Grandjean, "Imaging nonradiative point defects buried in quantum wells using cathodoluminescence," *Nano Lett.* **21**, 5217–5224 (2021).
- ³⁹K. L. Pey, J. C. H. Phang, and D. S. H. Chan, "Cathodoluminescence contrast of localized defects part II. Defect investigation," *Scanning Micro.* **9**, 367–380 (1995).
- ⁴⁰W. Shockley and W. T. Read, "Statistics of the recombinations of holes and electrons," *Phys. Rev.* **87**, 835–842 (1952).
- ⁴¹K. Lohnert and E. Kubalek, "The cathodoluminescence contrast formation of localized non-radiative defects in semiconductors," *Phys. Status Solidi A* **83**, 307–314 (1984).
- ⁴²H. C. Casey, D. D. Sell, and K. W. Wecht, "Concentration dependence of the absorption coefficient for *n* and *p* type GaAs between 1.3 and 1.6 eV," *J. Appl. Phys.* **46**, 250–257 (1975).
- ⁴³K. Nordlund, J. Peltola, J. Nord, J. Keinonen, and R. S. Averback, "Defect clustering during ion irradiation of GaAs: Insight from molecular dynamics simulations," *J. Appl. Phys.* **90**, 1710–1717 (2001).

- ⁴⁴J. H. Warner, S. R. Messenger, R. J. Walters, G. P. Summers, M. J. Romero, and E. A. Burke, "Displacement damage evolution in GaAs following electron, proton and silicon ion irradiation," *IEEE Trans. Nucl. Sci.* **54**, 1961–1968 (2007).
- ⁴⁵J. H. Warner, C. Inguibert, M. E. Twigg, S. R. Messenger, R. J. Walters, M. J. Romero, and G. P. Summers, "Effect of proton and silicon ion irradiation on defect formation in GaAs," *IEEE Trans. Nucl. Sci.* **55**, 3016–3024 (2008).
- ⁴⁶H.-L. Chen, A. Scaccabarozzi, R. De Lépinau, F. Oehler, A. Lemaître, J.-C. Harmand, A. Cattoni, and S. Collin, "Quantitative assessment of carrier density by cathodoluminescence. I. GaAs thin films and modeling," *Phys. Rev. Appl.* **15**, 024006 (2021).
- ⁴⁷U. Aeberhard, "Impact of built-in fields and contact configuration on the characteristics of ultra-thin GaAs solar cells," *Appl. Phys. Lett.* **109**, 033906 (2016).
- ⁴⁸M. van Eerden, J. Gastel, G. J. Bauhuis, P. Mulder, E. Vlieg, and J. J. Schermer, "Observation and implications of the Franz-Keldysh effect in ultrathin GaAs solar cells," *Prog. Photovolt. Res. Appl.* **28**, 779–787 (2020).
- ⁴⁹J. Shi-Rong, X. Zhong-ying, L. Jin-sheng, L. Chang-ping, X. Ji-zong, and Z. Bao-zhen, "Well-width dependence of the exciton lifetime in GaAs/AlGaAs quantum wells," *Acta Phys. Sin. (Overseas Edn)* **3**, 384–389 (1994).
- ⁵⁰G. Summers, R. Walters, M. Xapsos, E. Burke, S. Messenger, P. Shapiro, and R. Statler, "A new approach to damage prediction for solar cells exposed to different radiations," in *Proceedings of 1994 IEEE 1st World Conference on Photovoltaic Energy Conversion—WCPEC (A Joint Conference of PVSC, PVSEC and PSEC)* (IEEE, Piscataway, NJ, 1994), Vol. 2, pp. 2068–2075.
- ⁵¹A. Barry, A. Houdayer, P. Hinrichsen, W. Letourneau, and J. Vincent, "The energy dependence of lifetime damage constants in GaAs LEDs for 1–500 MeV protons," *IEEE Trans. Nucl. Sci.* **42**, 2104–2107 (1995).
- ⁵²M. Parenteau, C. Carlone, D. Morris, and S. Khanna, "Time-resolved spectroscopy of irradiated n-GaAs," *IEEE Trans. Nucl. Sci.* **44**, 1849–1855 (1997).
- ⁵³V. Kalinovsky, V. Andreev, V. Evstropov, V. Khvostikov, and V. Lantratov, "The recombination and tunnel current in GaAs-based solar cells: effect of radiation," in *Proceedings of 3rd World Conference on Photovoltaic Energy Conversion, 2003* (IEEE, Piscataway, NJ, 2003), Vol. 1, pp. 765–768.
- ⁵⁴M. Turowski, T. Bald, A. Raman, A. Fedoseyev, J. H. Warner, C. D. Cress, and R. J. Walters, "Simulating the radiation response of GaAs solar cells using a defect-based TCAD model," *IEEE Trans. Nucl. Sci.* **60**, 2477–2485 (2013).
- ⁵⁵M. Sotoodeh, A. H. Khalid, and A. A. Rezazadeh, "Empirical low-field mobility model for III–V compounds applicable in device simulation codes," *J. Appl. Phys.* **87**, 2890–2900 (2000).
- ⁵⁶J. U. Patel, J. G. Williams, and G. E. Stillman, "Degradation of mobility in neutron irradiated GaAs by the increased scattering from multiply charged ionized defects," *J. Appl. Phys.* **73**, 3734–3739 (1993).
- ⁵⁷A. Jorio, M. Parenteau, M. Aubin, C. Carlone, S. Khanna, and J. Gerdes, "A mobility study of the radiation induced order effect in gallium arsenide," *IEEE Trans. Nucl. Sci.* **41**, 1937–1944 (1994).
- ⁵⁸A. Sagatova, V. Krsjak, S. Sojak, O. Riabukhin, E. Kovacova, and B. Zatko, "Semi-insulating GaAs detectors degraded by 8 MeV electrons up to 1500 kGy," *J. Inst.* **16**, C12032 (2021).
- ⁵⁹J. H. Warner, G. P. Summers, R. J. Walters, and S. R. Messenger, "Energy dependence of majority carrier defect introduction rates in p+ n GaAs photodiodes irradiated with protons," *J. Appl. Phys.* **96**, 7225–7228 (2004).
- ⁶⁰V. L. Dalal, A. B. Dreeben, and A. Triano, "Temperature dependence of hole velocity in p-GaAs," *J. Appl. Phys.* **42**, 2864–2867 (1971).
- ⁶¹J. Ruch, "Electron dynamics in short channel field-effect transistors," *IEEE Trans. Electron Dev.* **19**, 652–654 (1972).
- ⁶²J. Son, W. Sha, J. Kim, T. B. Norris, J. F. Whitaker, and G. A. Mourou, "Transient velocity overshoot dynamics in GaAs for electric fields ≤ 200 kV/cm," *Appl. Phys. Lett.* **63**, 923–925 (1993).
- ⁶³C.-T. Sah, R. Noyce, and W. Shockley, "Carrier generation and recombination in P-N junctions and P-N junction characteristics," *Proc. IRE* **45**, 1228–1243 (1957).
- ⁶⁴E. D. Kosten, B. M. Kayes, and H. A. Atwater, "Experimental demonstration of enhanced photon recycling in angle-restricted GaAs solar cells," *Energy Environ. Sci.* **7**, 1907–1912 (2014).
- ⁶⁵J. S. Blakemore, "Semiconducting and other major properties of gallium arsenide," *J. Appl. Phys.* **53**, R123–R181 (1982).
- ⁶⁶C. Pellegrino, A. Gagliardi, and C. G. Zimmermann, "Difference in space-charge recombination of proton and electron irradiated GaAs solar cells," *Prog. Photovolt. Res. Appl.* **27**, 379–390 (2019).
- ⁶⁷X. J. Chen, H. J. Barnaby, J. H. Warner, S. R. Messenger, R. J. Walters, S. A. Ringel, and J. Park, "Non-linear behaviors of dark current slope in P+N GaAs solar cells following proton irradiations," in *2009 34th IEEE Photovoltaic Specialists Conference (PVSC)* (IEEE, Philadelphia, PA, 2009), pp. 001565–001570.
- ⁶⁸O. Breitenstein, J. Bauer, A. Lotnyk, and J.-M. Wagner, "Defect induced non-ideal dark- characteristics of solar cells," *Superlatt. Microstruct.* **45**, 182–189 (2009).
- ⁶⁹S. Steingrube, O. Breitenstein, K. Ramspeck, S. Glunz, A. Schenk, and P. P. Altermatt, "Explanation of commonly observed shunt currents in c-Si solar cells by means of recombination statistics beyond the Shockley-Read-Hall approximation," *J. Appl. Phys.* **110**, 014515 (2011).
- ⁷⁰A. Schenk and U. Krumbein, "Coupled defect-level recombination: Theory and application to anomalous diode characteristics," *J. Appl. Phys.* **78**, 3185–3192 (1995).
- ⁷¹D. Zhu, J. Xu, A. N. Noemaun, J. K. Kim, E. F. Schubert, M. H. Crawford, and D. D. Koleske, "The origin of the high diode-ideality factors in GaInN/GaN multiple quantum well light-emitting diodes," *Appl. Phys. Lett.* **94**, 081113 (2009).
- ⁷²J. Kim, Y. Tak, J. Kim, S. Chae, J.-Y. Kim, and Y. Park, "Analysis of forward tunneling current in InGaN/GaN multiple quantum well light-emitting diodes grown on Si (111) substrate," *J. Appl. Phys.* **114**, 013101 (2013).
- ⁷³M. Mandurriño, G. Verzellesi, M. Goano, M. Vallone, F. Bertazzi, G. Ghione, M. Meneghini, G. Meneghesso, and E. Zanoni, "Physics-based modeling and experimental implications of trap-assisted tunneling in InGaN/GaN light-emitting diodes: Physics-based modeling and experimental implications of TAT in InGaN/GaN LEDs," *Phys. Status Solidi A* **212**, 947–953 (2015).
- ⁷⁴U. Aeberhard, "Nonequilibrium Green's function picture of nonradiative recombination of the Shockley-Read-Hall type," *Phys. Rev. B* **99**, 125302 (2019).
- ⁷⁵P. A. White, "A coverglass for GaAs solar cells," in *IEEE Conference on Photovoltaic Specialists*, Vol. 2 (IEEE, Kissimmee, FL, 1990), pp. 1300–1303.
- ⁷⁶F. Lei, R. Truscott, C. Dyer, B. Quaghebeur, D. Heynderickx, R. Nieminen, H. Evans, and E. Daly, "MULASSIS: A geant4-based multilayered shielding simulation tool," *IEEE Trans. Nucl. Sci.* **49**, 2788–2793 (2002).